



THE 2ND ASIA-PACIFIC INTERNATIONAL CONFERENCE ON ADDITIVE MANUFACTURING (APICAM 2019)

Probing Ultrafast Dynamics in Laser Powder Bed Fusion Using High-Speed X-Ray Imaging: A Review of Research at the Advanced Photon Source

TAO SUN ^{1,2}

1.—Department of Materials Science and Engineering, University of Virginia, Charlottesville, VA, USA. 2.—e-mail: ts7qw@virginia.edu

Additive manufacturing (AM) is a transformative technology that opens up many exciting opportunities. In metal AM processes, high-power heat sources are often used to locally fuse the metal feedstock to the previous layer. Extreme thermal conditions are involved and unique microstructures are developed in AM-processed materials. At the Advanced Photon Source, we applied high-speed x-ray imaging to probe the ultrafast dynamics of the vapor depression, melt flow and particle spattering, among other transient phenomena. Demonstrated by the scientific cases reviewed and cited here, high-speed x-ray imaging is a unique tool for metal AM research. It provides invaluable information that can help address the critical issues in AM associated with structural defects, high-fidelity models, build reliability and repeatability.

INTRODUCTION

Additive manufacturing (AM), in contrast to subtractive manufacturing (i.e., cutting, milling, drilling, etc.), refers to a suite of disruptive technologies that build three-dimensional objects by adding feedstock materials layer by layer based on digital designs. AM has many advantages over conventional techniques, such as the increased complexity of parts, high customization, short supply chain, on-site and on-demand production, reduction of material and energy consumption, etc. These characteristics are highly favorable for the next-generation “smart factory,” and thus AM is regarded as one of the major forces that can lead us to the next industry revolution. Indeed, since AM largely unleashes design freedom, engineers are now able to build topologically optimized parts with superior performance that could never be achieved before.¹

Metal printing is an important area in AM. Because of the mentioned advantages, metal AM has found extensive applications in the aerospace, automobile, medical, defense and energy industries. More importantly, metal AM technologies opened up tremendous opportunities for fabricating novel non-equilibrium metallic and composite systems as

well as functionally graded architectures.^{2,3} Private sectors have been heavily investing in AM, shown by the facts that new original equipment manufacturers (OEMs) are emerging every year, and the number of companies that adopt AM technologies for making products and tools is increasing rapidly. However, building defect-free metal parts with precisely controlled microstructures and the desired performance remains challenging, largely because many fundamental problems in metal AM have not been solved yet. In addition to the specific challenges associated with different material systems, there are three common issues that need to be addressed before AM can truly change the way we make things: (1) a variety of structural defects that degrade the material properties; (2) limited materials that print well; (3) poor reliability and repeatability over time and across build platforms.

At the Advanced Photon Source (APS) of Argonne National Laboratory, our team, together with collaborators across the world, recently developed and applied a high-speed synchrotron x-ray imaging technique for in situ characterization of various metal AM processes.⁴⁻⁷ The high penetration power of hard x-rays makes it possible to look into dense metallic materials and watch their dynamic structural evolution during AM processes. Many highly

transient processes involved in metal AM were quantitatively measured with unprecedented spatial and temporal resolutions, and the mechanisms responsible for different types of defects in AM materials were identified. In this contribution, the high-speed x-ray imaging technique and beamline instrument for laser powder bed fusion (LPBF) research will be introduced, followed by two scientific cases that highlight the new understanding gained from synchrotron x-ray imaging experiments. The impact of x-ray studies on the development of AM materials, processes and numerical models will be summarized at the end.

EXPERIMENTAL DETAILS

High-Speed X-Ray Imaging Beamline

The high-speed x-ray imaging experiments were performed at the 32-ID-B beamline of the APS. Two undulators are installed to generate high-flux polychromatic x-rays (i.e., “white” beam). The U18 undulator has a relatively short period (i.e., 1.8 cm), which produces a pseudo “pink” beam with the first harmonic of the x-rays containing > 90% total flux. The energy of the first harmonic is in the range of 23.7–25.7 keV depending on the undulator gap setting, and the energy bandwidth is about 3–7% controlled by the white beam slits. Figure 1a shows the inside of the beamline. The hutch is about 9 m long and 4 m wide, large enough to accommodate complex *operando* systems. The samples are generally located 35–38 m downstream from the source. The full x-ray beam size at the sample location is about 2 mm × 2 mm, which can be further collimated down using slits. The critical components of the beamline include a set of slow shutters, one or two sets of fast shutters and a high-speed camera system. The slow shutters consist of

two pieces of water-cooled copper blocks that can take the heat load induced by the intense white beam. Once triggered, the slow shutters move in vertical motion (~ 50 ms to fully open) to control the passing of the x-ray beam. The fast shutters are made of small Pb pieces. Their opening time is on the scale of 500 μ s, sufficiently short for defining the x-ray time window with ms precision. A He-filled flight path is available between the shutters and the sample, which is used for reducing the air scattering of the incident x-ray beam. It helps improve the image quality, particularly when low-energy x-rays are used. The high-speed camera system integrates a scintillator (100- μ m-thick $\text{Lu}_3\text{Al}_5\text{O}_{12}:\text{Ce}$), a 45° reflection mirror behind the scintillator, an objective lens and a high-speed visible-light camera (Photron FastCam SA-Z). In most AM experiments, a 10× objective lens was used, providing a nominal imaging resolution of 2 μ m/pixel.

Laser Additive Manufacturing Simulator

The laser AM simulator is a home-built system, which is capable of generating the conditions used in real-world LPBF processes (Fig. 1b).⁵ Multiple components are vertically integrated and mounted on a small optic table. The reduced footprint makes it easy to install the system in other APS beamlines for different experiments. The laser source is a single-mode 1070-nm fiber laser with a maximum power of ~ 500 W (IPG YLR-500-AC). It can run in both continuous-wave (CW) mode and pulsed mode (maximum rate of 50 kHz). The scanner is a galvanometer scanner (SCANLAB, model IntelliSCANde 30), delivering a maximum scan speed of ~ 2 m/s. A F-Theta objective lens (f/340 mm) focuses the laser beam to ~ 50 μ m at its focal plane. The scanner is also equipped with a small inline

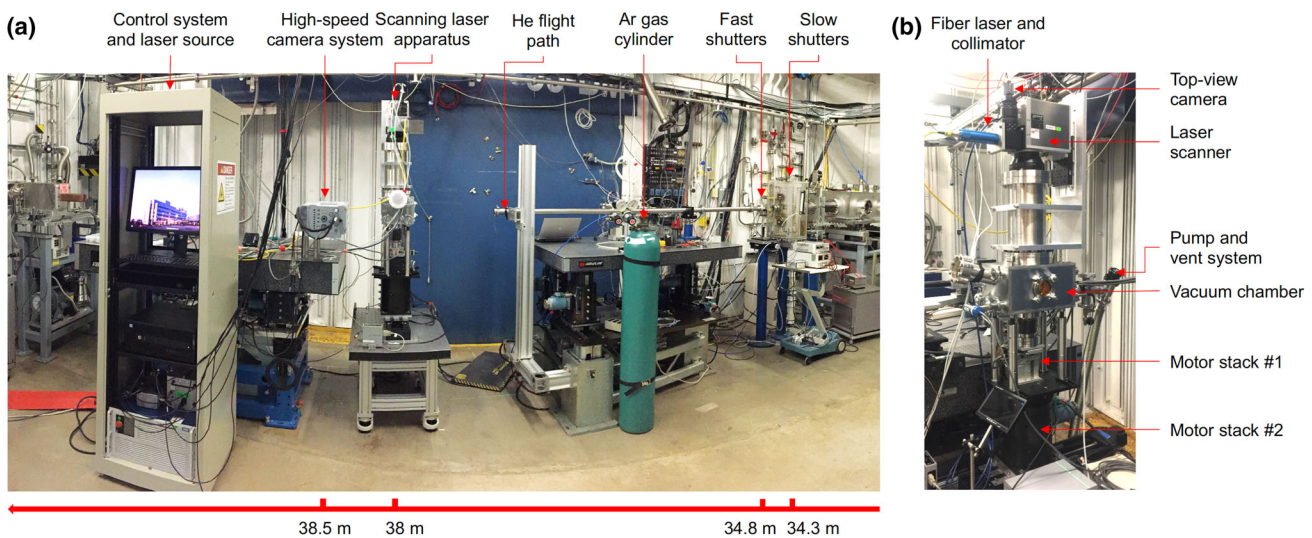


Fig. 1. (a) Photo of the 32-ID-B beamline. (b) Photo of the laser additive manufacturing simulator.

CCD camera, which provides the top view of the sample to facilitate the sample-laser alignment.

The sample vacuum chamber is made of half-inch stainless steel. A fused-silica window (diameter 152.4 mm) is mounted at the top of the column to allow laser entrance. There are multiple windows, viewports and feedthroughs on the chamber. The x-ray entrance and exit windows are made of 100- μ m-thick Kapton foils. There is an CaF_2 window at the outboard side of the chamber for angle-view infrared and visible-light imaging. The pumping and venting system can be connected to either side of the chamber to accommodate different beamline configurations. The sample stage is mounted on a X–Y–Z motor stack for fine position maneuvers, with X being the horizontal direction perpendicular to the x-ray beam, Y being the vertical direction and Z being the x-ray incidence direction. There is another set of heavy-duty X–Y motors underneath the sample chamber. They are used to move the chamber and scanner together for aligning the system with the x-ray beam and adjusting the on-sample laser spot size.

RESULTS AND DISCUSSION

Representative High-Speed X-Ray Images of Laser Powder Bed Fusion

LPBF is one of the most extensively used metal AM techniques. It is not a complex process conceptually: a thin layer of powder is spread evenly onto the base plate, and a laser beam is scanned across the powder bed in pre-defined paths, melting the powders locally and fusing them to the bottom layer; after printing one layer, the same procedure is repeated for the following layers. This seemingly simple process involves rather extreme thermal conditions: (1) The maximum local temperature of the sample is often higher than the boiling point of the metal being processed, leading to strong vaporization of metals, as will be elaborated later. (2) The heating and cooling rates are generally in the orders of 10^5 – 10^6 K/s. (3) The thermal gradient inside the melt pool can reach 10^3 K/mm. This extreme condition induces many highly dynamic and transient physical processes, including but not limited to melt flow driven by strong recoil pressure and Marangoni convection; powder flow and spattering induced by metal vapor and ambient gas; fluctuation of vapor depression associated with local laser absorption and reflection; rapid solidification and kinetics-controlled phase transformation. The complex interplay among these dynamic processes often results in structure defects in the build, such as rough surface, porosity, cracks, residual stress, and undesired phase and grain structures, which are detrimental to part performance.

Using high-speed x-ray imaging, the dynamic laser-material interaction could be captured with micrometer spatial resolution and microsecond temporal resolution. Figure 2 shows a representative

image series of the LPBF process of an Al-10Si-Mg sample. The data were collected with a frame rate of 30,173 fps and an exposure time of 100 ps for each image. As detailed below, many dynamic structure signatures can be measured quantitatively from these high-resolution x-ray images. The physics associated with these structural attributes as well as their implication for the printing process will be discussed in the following sections.

The vapor depression (*a.k.a.* keyhole) is the high-contrast zone underneath the laser beam, as indicated by a yellow arrow in Fig. 2a. In the LPBF processes, the powder density of the laser beam is generally high enough to vaporize the material locally. The recoil pressure induced by the vaporization thus creates a depression in the melt pool. Measuring the morphology and dynamics of the vapor depression is critical for estimating the laser absorptivity of the sample and also for studying the particle-spattering behavior and keyhole porosity generation. The melt pool (indicated by a red arrow in Fig. 2a and marked in red in Fig. 2b, c, d, e and f) is another important structural signature in metal AM. It connects the laser energy input with the final microstructure of the sample. Although the fine structure of the mushy zone does not show discernible contrast in x-ray images, the site- and time-specific solidification rates can be measured, which allows us to understand some of the unique microstructures in the LPBF-processed materials. It is worth pointing out here that both the vapor depression and melt pool are sub-surface structures, and high-speed synchrotron x-ray imaging is by far the most effective technique for measuring their morphologies in situ and in real time. Another important phenomenon in LPBF is particle spattering. Because of the intense metal vapor plume arising from the depression zone, many particles are ejected from the melt pool and powder bed. Unlike the vapor depression and melt pool, spattering appears to be a phenomenon at or above the surface, which could be captured using optical cameras. However, the limited depth of focus of the objective lens in optical imaging systems poses a serious challenge for data analysis. Since the particles are ejected in different directions with high velocities, many of them could soon fly out of the focal plane of the lens and thereby become blurred in the optical images. A multi-camera system viewing from different angles may mitigate this issue, but analyzing the morphologic change of each particle based on optical images is still difficult. X-ray imaging does not experience this out-of-focus problem because the objective lens in the x-ray detection system is focused on the scintillator plane rather than the sample plane.

Transition from Conduction to Keyhole Mode Melting

The first scientific case presented here concerns the melting mode of metals, i.e., how a sample

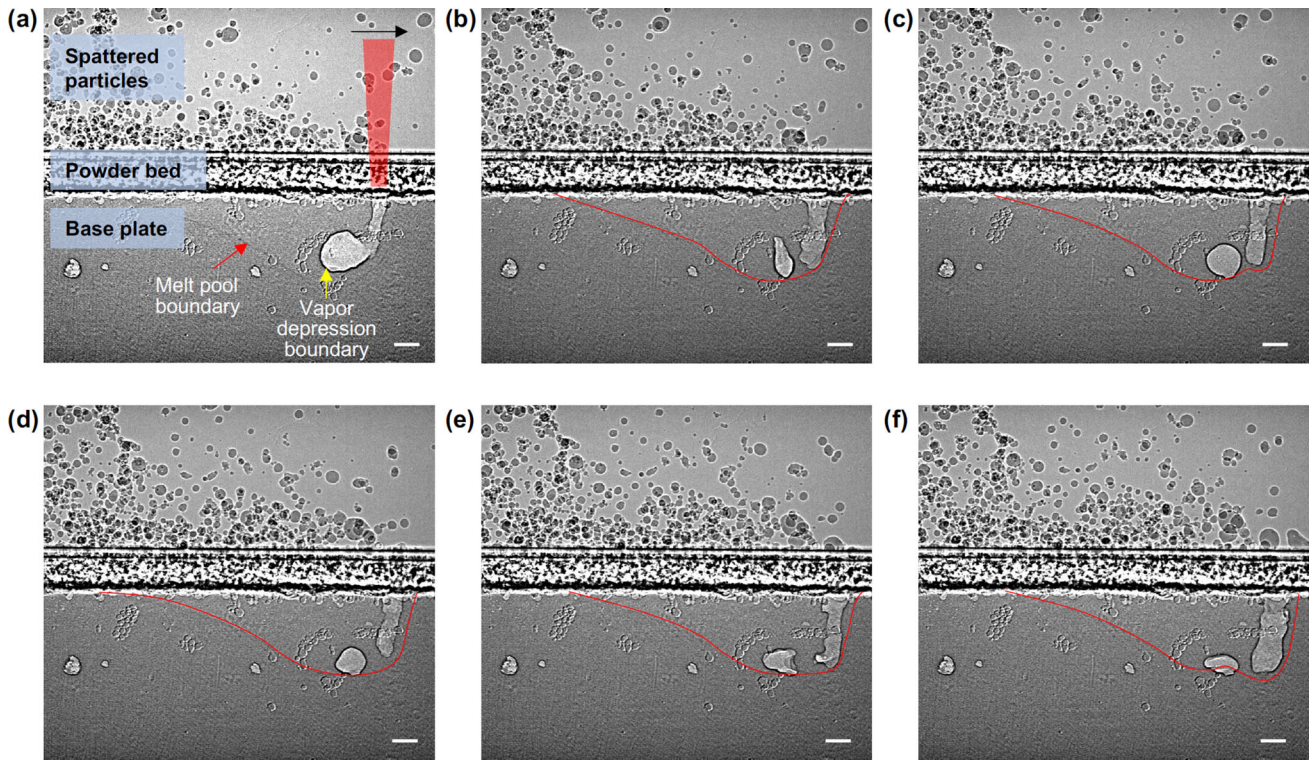


Fig. 2. Representative high-speed x-ray images of LPBF of Al-10Si-Mg. The frame rate is 30,173 fps, and the exposure time for each image is 100 ps. In (a), the laser beam position is illustrated in red, scanning from left to right. In (b–f), the melt pool boundaries are tracked using red lines. These six consecutive frames reveal the dynamics of the particle spattering, vapor depression and melt pool as well as the formation of a keyhole pore. The laser power is 540 W, scan speed is 0.6 m/s, and spot size is 80 μm . The powder size is 5–45 μm . All scale bars represent 100 μm (Color figure online).

absorbs the laser energy to develop a melt pool. Two modes of laser melting are generally used by the welding community: conduction and keyhole. These terms were later adopted by the AM community. It is convenient to explain these two modes in the case of a stationary laser. In conduction mode, no metal evaporation is involved; the heat transfer is primarily through conduction from the laser heating spot to the surrounding volume. The melt pool is believed to have a semi-spherical shape. In keyhole mode, the laser power density is high enough to boil the metal locally. The vapor recoil pressure then creates a cavity or depression in the melt pool, as we described previously. This depression zone can continue to grow, primarily in the depth direction, with continuous laser heating. Within this narrow and deep depression zone, the incident laser beam experiences multiple reflections by the walls. Since multiple absorption occurs in keyhole mode, the effective laser absorptivity is much higher than that in conduction mode. The term “keyhole” came from the shape of the melt pool (characterized by post cross-sectional microscopy), which has a semi-sphere on the top and a long narrow spike at the bottom, resembling the keyhole of an old warded lock.

In laser welding and drilling, the keyhole condition is routinely applied. In metal AM, based on

welding experience, there is motivation to avoid keyholing at all costs as it is believed that porosity in the build is associated with keyholes. This is only partially true as will be explained below. In fact, understanding of keyhole mode melting is limited and mostly qualitative, owing to the lack of in situ measurements. Some modeling efforts tried to define these two modes in more quantitative ways, yet experimental proof was scarce. In the study performed by a collaborative team from Carnegie Mellon University and Argonne National Laboratory, high-speed x-ray imaging was used to directly probe the dynamic morphologic evolution of the vapor depression and melt pool. The stationary laser experiments revealed that there are five distinct regimes of behavior: (1) melting, (2) vapor depression formation and growth, (3) vapor depression instability, (4) keyhole formation and growth and (5) melt pool shape change.⁸

Figure 3a shows a tableau of keyhole images in the P–V space (i.e., laser power–scan velocity) of Ti-6Al-4V bare plate samples. In the scanning laser case, the morphologies of vapor depressions vary largely across the P–V space. The high-resolution x-ray images collected in the stationary laser experiments allow the team to quantify the dimensions of the melt pool and keyhole. In the plot of keyhole depth versus time and the plot of the melt pool

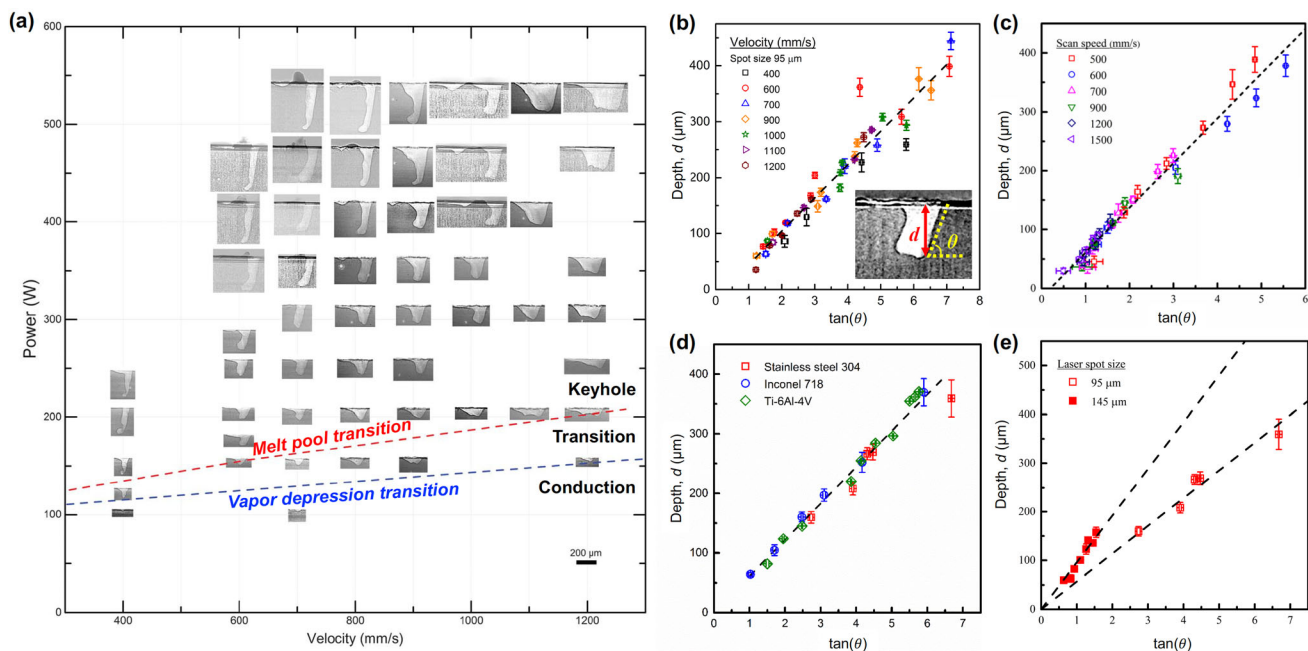


Fig. 3. (a) Tableau of representative radiographs in P–V space, showing the variation in vapor depression size and morphology. (b–e) Keyhole depth as a function of the tangent of the front keyhole wall angle in the cases of (b) bare plate samples, (c) powder bed samples, (d) different materials and (e) different laser spot sizes. The keyhole depth d and front wall angle θ are illustrated in the inset of (b). For powder bed samples, the keyhole depth d refers to the vapor depression depth inside the base plate. If not specified, the data were collected from Ti-6Al-4V samples and the laser spot size was 95 μm. Reprinted with permission from Ref. [8] (Color figure online).

depth-to-width ratio versus time, two clear transitions could be identified. The first one occurs as the vapor depression depth suddenly increases, and the second transition occurs later in the melt pool geometry plot, suggesting a change in heat absorption and transfer. These two transition times could be described as functions of the laser power density and re-plotted in the scanning laser P–V space (Fig. 3a). If the first transition is referred to as “vapor depression transition” (blue dashed line), the conditions in the P–V space below this line are in conduction mode. The second transition could be understood as “melt pool transition” (red dashed line in P–V space), where the shape of the melt pool starts to change to be “keyhole” like. Therefore, the laser conditions above this line all fall into the category of keyhole mode melting. The domain between these two lines can then be described as the “transition” zone. Interestingly, most of the conditions used in practical LPBF processes are actually within the keyhole zone. This is the case for both bare plate and powder bed samples.

Another interesting result is that the depth of the keyhole (d) follows a very simple relationship with its front wall angle (θ) as $d = D \cdot \tan \theta$, where D is the laser spot size (Fig. 3b). This can be understood as a geometric relationship, meaning once the laser has enough powder density to drill into the sample to form a stable keyhole, the whole incident laser beam will fall onto the front keyhole wall. This relationship was proposed by Fabbro more than 20 years ago, embedded in one of his modeling

works,⁹ but was never verified in an experiment with direct measurement of the keyhole morphology. For the powder bed samples, this linear relationship also holds well, with only a small shift toward lower keyhole depth (Fig. 3c).

With high-resolution x-ray imaging of the laser-metal interaction, the melting modes concerning the LPBF process can be defined in a much more rigorous way than ever before. In stable keyhole melting mode, the keyhole depth and front wall angle follow a simple geometric relationship that applies to all materials (Fig. 3d). A surprising fact is that the widely used processing window for building parts without major porosity is actually in keyhole condition. This is because the morphology of a stable keyhole does not fluctuate much during the build, and thus porosity is not prone to form. Moreover, since the keyhole depth is sensitive to the laser spot size (Fig. 3e), the laser beam of the printers needs to be calibrated routinely to assure good reliability and repeatability.

Particle Spattering

The second scientific advancement enabled by the high-speed x-ray imaging concerns the spattering phenomenon. Laser-induced spattering refers to the ejections of molten metal from a pool heated by a high-power stationary or scanning laser. In LPBF, particle spattering is almost inevitable because of the existence of a strong metal vapor. The flying hot particles may collide with each other and/or with

cold particles. These newly formed particles tend to have different compositions, microstructures and morphologies than the feedstock powders, creating problems for powder recycling. Moreover, when the spattered particles fall back onto the powder bed, they can negatively impact the build process. For instance, the larger particles can sometimes result in streaks in the powder bed during the recoating process, plus those particles or clusters with irregular shapes have poor flowability, creating conditions for lack-of-fusion defects.

As discussed earlier, x-ray imaging is a unique technique for studying the spattering phenomenon, because it does not experience the out-of-focus issue. A team from Missouri University of Science and Technology and Argonne National Laboratory has been studying the particle-spattering behavior in LBPF using high-speed x-ray imaging. One of the early work was focused on understanding the influence of ambient pressure on the in-bed and out-of-bed powder motions.¹⁰ The results of the stationary laser case are summarized in Fig. 4a and b. The powerful laser generates substantial metal vapor that escapes from the sample surface. The high-speed metal vapor then creates a zone around the laser beam where the gas pressure is lower than ambient because of the Bernoulli effect, and the ambient Ar gas will then carry powders to flow toward this low-pressure zone. Once interacting with the metal vapor plume, the trajectories of these powders will be altered (Fig. 4a1–a6 and b1–b4). Under the vacuum condition, since the Ar gas flow is absent, powders are simply blasted away from the powder bed by the metal vapor and fly in all directions (Fig. 4a7–a9 and b5–b6).

This work, as well as research by others,¹¹ managed to gain some general understanding of the laser-induced metal-spattering phenomenon. The proposed mechanisms are mostly concerned with the local laser energy absorption, vapor plume dynamics and melt flow. The complex interactions among the recoil pressure, vapor plume impact and surface tension of the molten metal are identified as the major causes of spattering. However, because of the highly dynamic and transient nature of laser-matter interactions, the key physical processes that lead to the initial formation of spatters had not been completely understood, primarily held back by the lack of in situ characterization of sub-surface structures. Also, the explanation of the occurrence of extremely fast spatters (i.e., tens of meters per second) was still unclear.

To address these issues, the Missouri-Argonne team, together with scientists on computational mechanics from the University of Utah, applied MHz x-ray imaging and multi-physics modeling to observe and understand the ultrafast dynamics of the keyhole and melt pool.¹² As shown in Fig. 5a, multiple events occur sequentially that eventually lead to spattering. In brief, the key observations include: (1) a relatively slow scanning high-power

laser generates a narrow and deep keyhole (Fig. 5a1); (2) small protrusions form on the front keyhole wall and continue to flow down (Fig. 5a2 and a3); (3) the small protrusions alter the vapor pressure at the keyhole bottom, causing the keyhole morphology to change from the typical “J”-like shape to a reverse-triangle-like shape (Fig. 5a3 and a4); (4) the directional vapor plume from the keyhole bottom collides toward the front keyhole wall, which serves as a necessary condition for the formation of a giant tongue-like protrusion (Fig. 5a5 and a6); (5) this unique protrusion continues to grow, and a mini-keyhole forms on its top, which causes its catastrophic fall to the keyhole center (Fig. 5a7); (6) the sudden fall of this large protrusion, on one hand, largely increases the laser absorption on its top surface and, on the other hand, vigorously mixes the superheated and normal liquids. The irregular fluctuation in internal thermal and pressure structures then triggers the explosion of the tongue-like protrusion (Fig. 5a8); (7) when the exploded vapor and fine droplets land at the rims of the keyhole walls, thin melt ligaments form, rise, neck and eventually break up into spatters (Fig. 5a9–a12).

The identification of a bulk explosion is supported by three pieces of evidence: (1) the simulation shows the tongue-like protrusion receives much increased laser energy once it falls to the center of the laser beam; (2) the subsequent responses from the front and rear keyhole walls are almost simultaneous; (3) the keyhole wall (planes perpendicular to x-ray incidence) becomes roughened, indicating the impact by high-speed fine droplets. This explosion phenomenon has some of the key characteristics of the well-defined phase explosion and vapor explosion processes. However, a rigorous physical description of the bulk explosion remains a challenge due to the limited resolutions afforded by the current light sources.

As revealed by our study, laser-induced metal spattering intrinsically connects with keyhole stability. A small perturbation on the front keyhole wall can alter the laser absorption, which may potentially induce sequential events that lead to spattering. Also, our study confirms unambiguously that spattering tends to happen when strong melt flow and intense vapor exist. Therefore, an effective approach to mitigate spattering is to reduce the metal vapor and suppress the melt flows around the keyhole.

X-Ray Imaging Complementing Other AM Studies

Thanks to the superior penetration power of high-energy photons and the brilliant flux afforded by the third-generation synchrotron facility, the high-speed x-ray imaging detailed above is capable of capturing the sub-surface structural dynamics with extremely high spatial and temporal resolutions. Researchers now can tackle the critical material

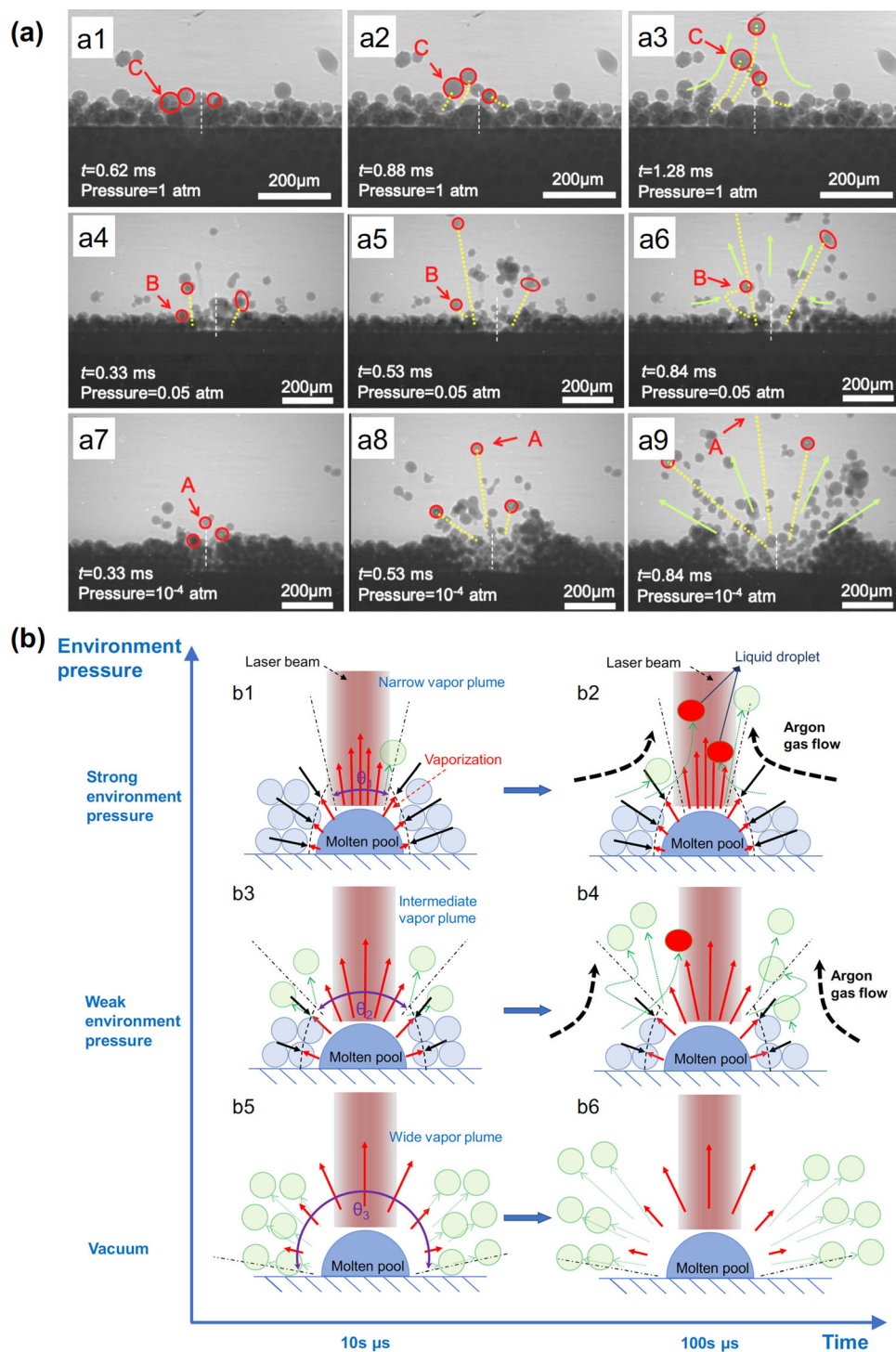


Fig. 4. (a) High-speed x-ray images showing powder motion at different moments and under different ambient Ar pressures in the case of stationary laser heating. The sample is 316L stainless steel. (b) Schematic summarizing powder-spattering behavior under different ambient Ar pressures. Reprinted with permission from Ref. [10].

problems associated with metal AM from a new and effective angle. In addition, the real-space morphologic information of the critical structure signatures can be used for calibrating and complementing AM data with other modalities. These data include, but are not limited to, in situ x-ray diffraction patterns,

thermal images and numerical simulations, as schematically illustrated in Fig. 6.

The high-speed full-field x-ray imaging technique relies on the density difference in materials to generate contrast in micrometer resolution, so it is not sensitive to the grain structures, dislocations,

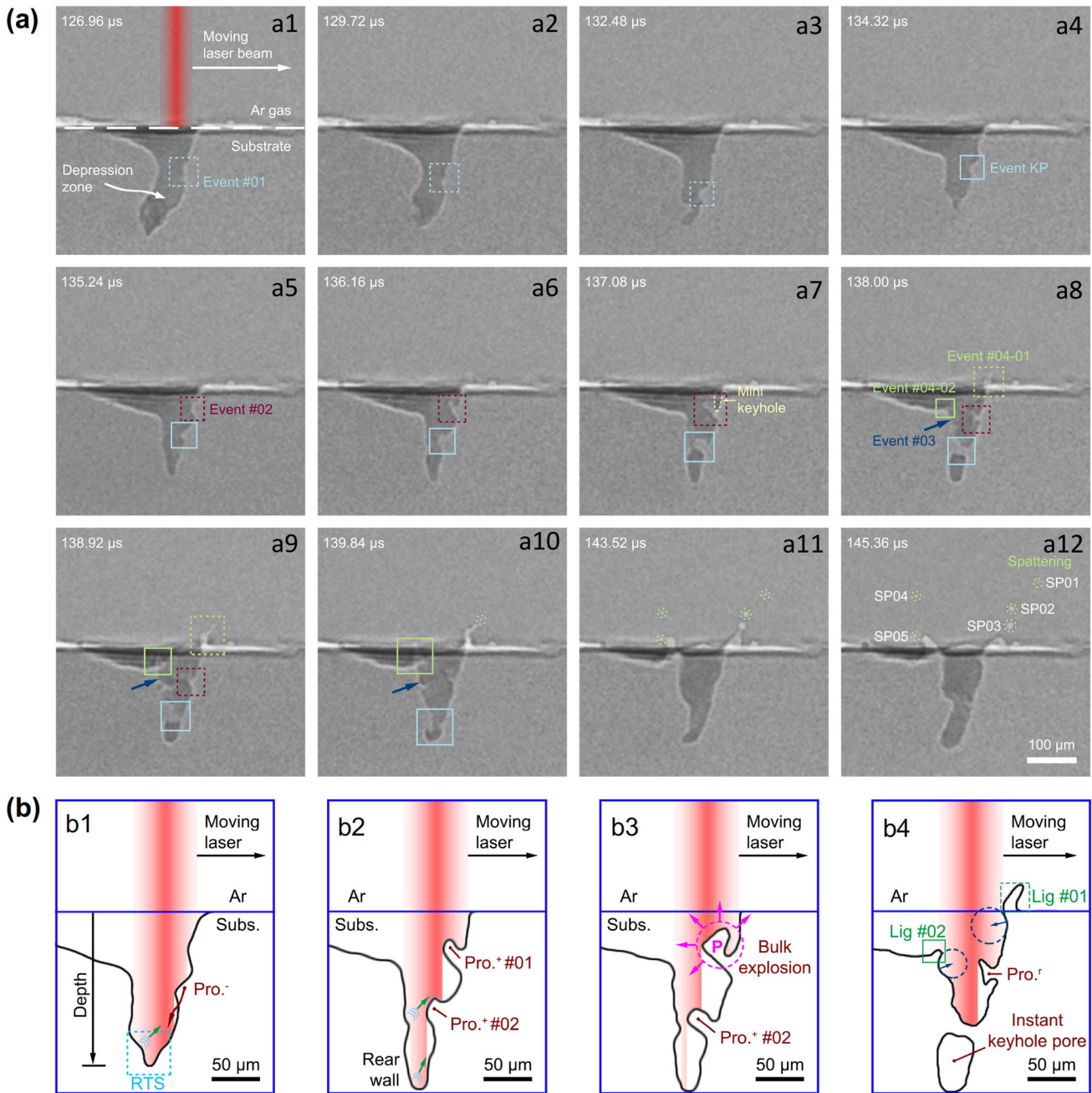


Fig. 5. (a) High-speed x-ray images revealing the sequential events in the melt pool that lead to the spattering in the case of scanning laser. The laser beam scans from left to right, with spot size of $\sim 80 \mu\text{m}$, power of 210 W and scanning speed of 500 mm/s. The frame rate is 1.087 million frames per second, synchronized with the x-ray pulses. Each individual image is generated by a single x-ray pulse ($\sim 100 \text{ ps}$). All images are background-corrected using the images collected before the laser melting. The sample is Ti-6Al-4V bare plate. (b) Schematic illustrations of the sequential events that lead to melt ligamentation. Adapted from Ref. [12].

nanoscale chemical segregation or phase of the materials. X-ray diffraction, on the other hand, can provide direct or indirect information on these important structural attributes. Therefore, research that utilizes imaging and diffraction tools together can potentially help scientists explain why AM materials contain very different microstructures than cast or wrought materials and why some metallic systems are not suitable for AM. In situ x-ray diffractions have been conducted at a few

high-energy beamlines at the APS. High-speed diffraction of Ti-6Al-4V using a “pink” x-ray was reported in one of the early works on technique development.⁴ The monochromatic diffraction data are being analyzed, and the results will be reported separately. Stress, temperature and chemical composition can all affect the lattice d -spacing of a crystalline material. Therefore, quantification of the lattice change due to these factors remains a major challenge.

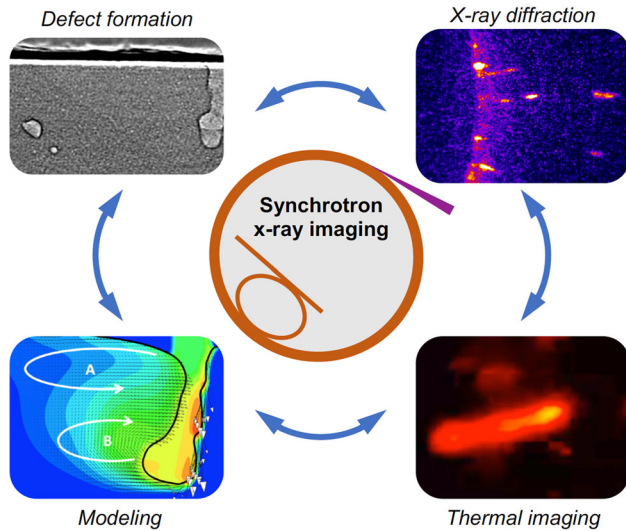


Fig. 6. Schematic with representative data showing the unique role of high-speed synchrotron x-ray imaging studies in advancing metal AM technologies, particularly LPBF. The simulation is reprinted with permission from Ref. [13].

Numerical models, such as thermal transfer, computational fluid dynamics, phase-field and multi-physics models, are frequently used for simulating AM processes and predicting the microstructures of the end product. Post-structural characterization has been used for verifying the fidelity of these models. Although this has been proved to be effective in many ways, more accurate initial inputs and boundary conditions measured from in situ experiments can certainly help improve the accuracy and robustness of the models. The morphologies of the vapor depression and melt pool measured by high-speed x-ray imaging serve this purpose nicely. On the other hand, modeling and simulation can provide information that cannot be measured experimentally (e.g., temperature distribution in the melt pool), which can help interpret the x-ray observations more quantitatively. In the work led by researchers at the University of Utah, a multi-physics model was developed that successfully reproduced the keyhole shapes under different laser conditions, observed in the high-speed x-ray imaging experiment. The distributions of laser absorption, temperature and flow velocity were calculated. In addition, the different forces (i.e., recoil pressure, capillary force and thermocapillary force) involved in the keyhole shape development and fluctuation were quantified.¹³ In another work led by researchers at Missouri University of Science and Technology, a multi-physics model was used for simulating the temperature distribution within the melt pool of an AlSi10Mg sample in LPBF. The simulation was validated by the vapor depression and melt pool morphologies observed in the x-ray imaging experiment while providing thermal information that could not be directly measured. The combination of experiment and modeling allowed the team to identify a novel mechanism for

eliminating porosity during LPBF, i.e., thermocapillary force-driven pore motion.¹⁴

To address the reliability issue of AM systems, there have been substantial efforts worldwide devoted to the development of in-process control systems. Such systems aim to monitor the printing process, analyzing the results in real time, and adjust the printing parameters accordingly. For instance, if an anomaly is detected, an effective feed-forward in-process control system can either stop the operation to save time and cost or inform the machine to correct the error in the next layer or next few layers. The commonly used sensory devices are visible-light cameras, thermal cameras and ultrasound sensors. Optical imaging can only capture the sample information on or above the surface. Ultrasound signals may detect the sample internal structure changes, but they could be difficult to interpret. Therefore, x-ray imaging can be used to calibrate sensory data with different modalities by providing unambiguous information on defect generation inside the sample.

SUMMARY

High-speed synchrotron x-ray imaging is a unique tool for metal AM research. The quantitative information on the complex transient processes involved in metal AM can not only help researchers understand the physics underlying the formation of different types of defects, but also inform and calibrate numerical models and other real-time monitoring data. The scientific cases introduced here are among many other interesting studies performed at the APS.^{15–20} Worldwide, more and more research teams have started to apply synchrotron x-ray imaging to address the critical issues associated with AM processes and materials. There are vibrant research activities at other synchrotron facilities, including Stanford Synchrotron Radiation Lightsource (SSRL), Diamond Light Source (DLS), European Synchrotron Radiation Facility (ESRF), Swiss Light Source (SLS) and Super Photon ring-8 GeV (Spring-8) facility, and the scope of research is still expanding. During the last 3 years, many new observations and understandings have been reported,^{21–27} which has largely enriched our fundamental knowledge on metal AM and facilitated the development and adoption of AM technologies. Owing to the higher flux of hard x-rays at high-energy synchrotron facilities (e.g., APS, ESRF, SPring-8), the temporal resolution of imaging experiments is usually higher than what is afforded by mid- or low-energy facilities. Currently, only APS and ESRF have beamlines that offer ultrahigh-speed multi-frame imaging capabilities (i.e., millions of frames per second and single x-ray pulse exposure). After the major upgrades of these hard x-ray facilities in the mid-2020s, the spatial/temporal resolutions and sensitivity of full-field imaging will be even higher. One could expect to see many more

details of the aforementioned dynamic processes in metal AM as well as new phenomena that we could not investigate now.

To the author's knowledge, research on electron beam-based AM techniques has not been reported. Probing melt pool dynamics in these AM processes is certainly of great interest, given that the complex beam motions in an e-beam system can result in different melt flow patterns and cooling behaviors of the materials. However, building an e-beam system for in situ x-ray experiments is more costly than a laser system, which may be why such experiments have not been carried out. After all, high-speed synchrotron x-ray imaging just started to be used for studying AM processes. There are still many challenges and opportunities in this research field, which call for substantial efforts from the community.

The direct impact of the high-speed x-ray imaging experiment can be summarized as follows. First, the direct observation of the AM process allows us to understand how various defects are generated and why some materials are difficult to print. Second, measurements of critical dynamic structural attributes can facilitate the development of high-fidelity models for simulating AM processes and materials. Third, x-ray allows us to see through a sample and watch its internal structure change during the AM processes. This can help validate other types of sensory data and contributes to the development of in-process monitoring and control systems. Collectively, the practitioners of AM technologies will be equipped with tools that allow them to perform research and development more effectively and efficiently than the conventional "Edisonian approach."

ACKNOWLEDGEMENTS

This contribution summarizes the content I presented at the 2019 Asia-Pacific International Conference on Additive Manufacturing. The research described here was all performed and published at the time I worked at the Advanced Photon Source. I would like to thank all our team members and collaborators for their great efforts, particularly Prof. Anthony Rollett at Carnegie Mellon University, Prof. Lianyi Chen at University of Wisconsin-Madison, and Prof. Wenda Tan at University of Utah, who led some of the projects I introduced in this contribution. All research described here used resources of the Advanced Photon Source, a US Department of Energy (DOE) Office of Science User Facility operated for the DOE Office of Science by Argonne National Laboratory under Contract No. DE-AC02-06CH11357.

REFERENCES

1. W.E. Frazier, *J. Mater. Eng. Perform.* 23, 1917 (2014).
2. T. DebRoy, H.L. Wei, J.S. Zuback, T. Mukherjee, J.W. Elmer, J.O. Milewski, A.M. Beese, A. Wilson-Heid, A. De, and W. Zhang, *Prog. Mater. Sci.* 92, 112 (2018).
3. D.D. Gu, W. Meiners, K. Wissenbach, and R. Poprawe, *Int. Mater. Rev.* 57, 133 (2012).
4. C. Zhao, K. Fezzaa, R.W. Cunningham, H. Wen, F. De Carlo, L. Chen, A.D. Rollett, and T. Sun, *Sci. Rep.* 7, 1 (2017).
5. N.D. Parab, C. Zhao, R. Cunningham, L.I. Escano, K. Fezzaa, W. Everhart, A.D. Rollett, L. Chen, and T. Sun, *J. Synchrotron Radiat.* 25, 1467 (2018).
6. N.D. Parab, J.E. Barnes, C. Zhao, R.W. Cunningham, K. Fezzaa, A.D. Rollett, and T. Sun, *Sci. Rep.* 9, 1 (2019).
7. S.J. Wolff, H. Wu, N. Parab, C. Zhao, K.F. Ehmann, T. Sun, and J. Cao, *Sci. Rep.* 9, 1 (2019).
8. R. Cunningham, C. Zhao, N. Parab, C. Kantzos, J. Pauza, K. Fezzaa, T. Sun, and A.D. Rollett, *Science (80-)* 363, 849 (2019).
9. R. Fabbro and K. Chouf, *J. Appl. Phys.* 87, 4075 (2000).
10. Q. Guo, C. Zhao, L.I. Escano, Z. Young, L. Xiong, K. Fezzaa, W. Everhart, B. Brown, T. Sun, and L. Chen, *Acta Mater.* 151, 169 (2018).
11. S. Ly, A.M. Rubenchik, S.A. Khairallah, G. Guss, and M.J. Matthews, *Sci. Rep.* 7, 1 (2017).
12. C. Zhao, Q. Guo, X. Li, N. Parab, K. Fezzaa, W. Tan, L. Chen, and T. Sun, *Phys. Rev. X* 9, 21052 (2019).
13. N. Kouraytem, X. Li, R. Cunningham, C. Zhao, N. Parab, T. Sun, A.D. Rollett, A.D. Spear, and W. Tan, *Phys. Rev. Appl.* 11, 1 (2019).
14. S.M.H. Hojjatzadeh, N.D. Parab, W. Yan, Q. Guo, L. Xiong, C. Zhao, M. Qu, L.I. Escano, X. Xiao, K. Fezzaa, W. Everhart, T. Sun, and L. Chen, *Nat. Commun.* 10, 1 (2019).
15. A. Bobel, L.G. Hector, I. Chelladurai, A.K. Sachdev, T. Brown, W.A. Poling, R. Kubic, B. Gould, C. Zhao, N. Parab, A. Greco, and T. Sun, *Materialia* 6, 100306 (2019).
16. Q. Guo, C. Zhao, M. Qu, L. Xiong, L.I. Escano, S.M.H. Hojjatzadeh, N.D. Parab, K. Fezzaa, W. Everhart, T. Sun, and L. Chen, *Addit. Manuf.* 28, 600 (2019).
17. B. Richter, N. Blanke, C. Werner, N.D. Parab, T. Sun, F. Vollertsen, and F.E. Pfefferkorn, *CIRP Ann.* 68, 229 (2019).
18. L.I. Escano, N.D. Parab, L. Xiong, Q. Guo, C. Zhao, K. Fezzaa, W. Everhart, T. Sun, and L. Chen, *Sci. Rep.* 8, 1 (2018).
19. N.D. Parab, L. Xiong, Q. Guo, Z. Guo, C. Kirk, Y. Nie, X. Xiao, K. Fezzaa, W. Everhart, W.W. Chen, L. Chen, and T. Sun, *Addit. Manuf.* 30, 100878 (2019).
20. Q. Guo, C. Zhao, M. Qu, L. Xiong, S.M.H. Hojjatzadeh, L.I. Escano, N.D. Parab, K. Fezzaa, T. Sun, and L. Chen, *Addit. Manuf.* 31, 100939 (2019).
21. Y. Kawahito and H. Wang, *Scr. Mater.* 154, 73 (2018).
22. C.L.A. Leung, S. Marussi, R.C. Atwood, M. Towrie, P.J. Withers, and P.D. Lee, *Nat. Commun.* 9, 1 (2018).
23. N.P. Calta, J. Wang, A.M. Kiss, A.A. Martin, P.J. Depond, G.M. Guss, V. Thampy, A.Y. Fong, J.N. Weker, K.H. Stone, C.J. Tassone, M.J. Kramer, M.F. Toney, A. Van Buuren, and M.J. Matthews, *Rev. Sci. Instrum.* 89, 055101 (2018).
24. C.L.A. Leung, S. Marussi, M. Towrie, J. del Val Garcia, R.C. Atwood, A.J. Bodey, J.R. Jones, P.J. Withers, and P.D. Lee, *Addit. Manuf.* 24, 647 (2018).
25. C.L.A. Leung, S. Marussi, M. Towrie, R.C. Atwood, P.J. Withers, and P.D. Lee, *Acta Mater.* 166, 294 (2019).
26. A.A. Martin, N.P. Calta, S.A. Khairallah, J. Wang, P.J. Depond, A.Y. Fong, V. Thampy, G.M. Guss, A.M. Kiss, K.H. Stone, C.J. Tassone, J. Nelson Weker, M.F. Toney, T. van Buuren, and M.J. Matthews, *Nat. Commun.* 10, 1 (2019).
27. A.A. Martin, N.P. Calta, J.A. Hammons, S.A. Khairallah, M.H. Nielsen, R.M. Shuttlesworth, N. Sinclair, M.J. Matthews, J.R. Jeffries, T.M. Willey, and J.R.I. Lee, *Mater. Today Adv.* 1, 100002 (2019).

Publisher's Note Springer Nature remains neutral with regard to jurisdictional claims in published maps and institutional affiliations.